NOAA Technical Report ERL 445–PMEL 40

Satellite Observations of Mesoscale Features in Lower Cook Inlet and Shelikof Strait, Gulf of Alaska

James D. Schumacher
Willard E. Barber
Benjamin Holt
Antony K. Liu

May 1991

U.S. DEPARTMENT OF COMMERCE
National Oceanic and Atmospheric Administration
Environmental Research Laboratories

NOAA Technical Report ERL 445–PMEL 40

Satellite Observations of Mesoscale Features in Lower Cook Inlet and Shelikof Strait, Gulf of Alaska

James D. Schumacher
Pacific Marine Environmental Laboratory

Willard E. Barber
University of Alaska at Fairbanks

Benjamin Holt
Jet Propulsion Laboratory

Antony K. Liu
NASA/Goddard Space Flight Center

Pacific Marine Environmental Laboratory
Seattle, Washington

May 1991

U.S. Department of Commerce
Robert A. Mosbacher, Secretary

National Oceanic and Atmospheric Administration
John A. Knauss, Under Secretary for Oceans and Atmosphere / Administrator

Environmental Research Laboratories
Boulder, Colorado
Joseph O. Fletcher, Director

NOTICE

Mention of a commercial company or product does not constitute an endorsement by NOAA/ERL. Use of information from this publication concerning proprietary products or the tests of such products for publicity or advertising purposes is not authorized.

Contribution No. 1230 from NOAA/Pacific Marine Environmental Laboratory

For sale by the National Technical Information Service, 5285 Port Royal Road
Springfield, VA 22161

CONTENTS

Satellite Observations of Mesoscale Features in Lower Cook Inlet and Shelikof Strait, Gulf of Alaska

James D. Schumacher, Willard E. Barber, Benjamin Holt, and Antony K. Liu

ABSTRACT. The Seasat satellite launched in summer 1978 carried a synthetic aperture radar (SAR). Although Seasat failed after 105 days in orbit, it provided observations that demonstrate the potential to examine and monitor upper oceanic processes. Seasat made five passes over lower Cook Inlet and Shelikof Strait, Alaska, during summer 1978. SAR images from the passes show oceanographic features, including a meander in a front, a pair of mesoscale eddies, and internal waves. These features are compared with contemporary and representative images from a satellite-borne Advanced Very High Resolution Radiometer (AVHRR) and Coastal Zone Color Scanner (CZCS), with water property data, and with current observations from moored instruments. The results indicate that SAR data can be used to monitor mesoscale oceanographic features.

1. INTRODUCTION

It is generally accepted that physical oceanic processes influence and may even be the primary determinant of the recruitment of fish to oceanic fisheries. In particular, the impacts of these processes on survival during the early life stages of fish as they are being transported from spawning grounds to nursery areas are believed to be the most important factors in determining recruitment (Rothchild, 1986). Mortality is affected by two broad categories of physical mechanisms: turbulence of the water column, which influences food availability, and fluctuations in current patterns transporting eggs and larvae to nursery areas. Currently, there is a long-term interdisciplinary program, Fisheries Oceanography Coordinated Investigations (FOCI), examining the influence of the environment in Shelikof Strait, Gulf of Alaska (Fig. 1), on survival and recruitment of walleye pollock (*Theragra chalcogramma*) to the fisheries (Reed et al., 1988). Results to date include identification of eddies (Incze et al., 1990; Vastano et al., 1991) and complex current patterns that affect transport (Schumacher et al., 1989) and dispersion (Reed et al., 1989) of larvae as they drift to nursery grounds along the Alaskan Peninsula (Hinckley et al., 1991).

Advanced Very High Resolution Radiometer (AVHRR) satellite images from the study area have been used to construct surface current distributions that are consistent with in situ current and water property measurements (Vastano et al., 1991). A marked feature of contemporary satellite and larval distribution data (Fig. 2) is that the greatest concentrations of larvae are situated in eddies. These results suggest that eddies may play a crucial role in retaining larvae on the shelf, thereby inhibiting transport into the Gulf of Alaska. A problem with AVHRR techniques in this region, however, is that cloud cover usually inhibits acquisition of clear imagery over a sufficiently large area to produce maps of surface temperature (Royer and Muench, 1977) and inferred currents. The advantage of imagery from synthetic aperture radar (SAR) over that from AVHRR is that it is unaffected by cloud cover. Additionally, the SAR is capable of producing imagery with a resolution as fine as 25 m, compared with the 1-km resolution of AVHRR. Over the ocean, SAR detects backscattered energy that is affected by the small-scale roughness arising from short surface waves. Variability in the short waves is produced by interactions with longer waves, currents, and atmospheric conditions to produce a fine-scale two-dimensional map of the ocean surface.

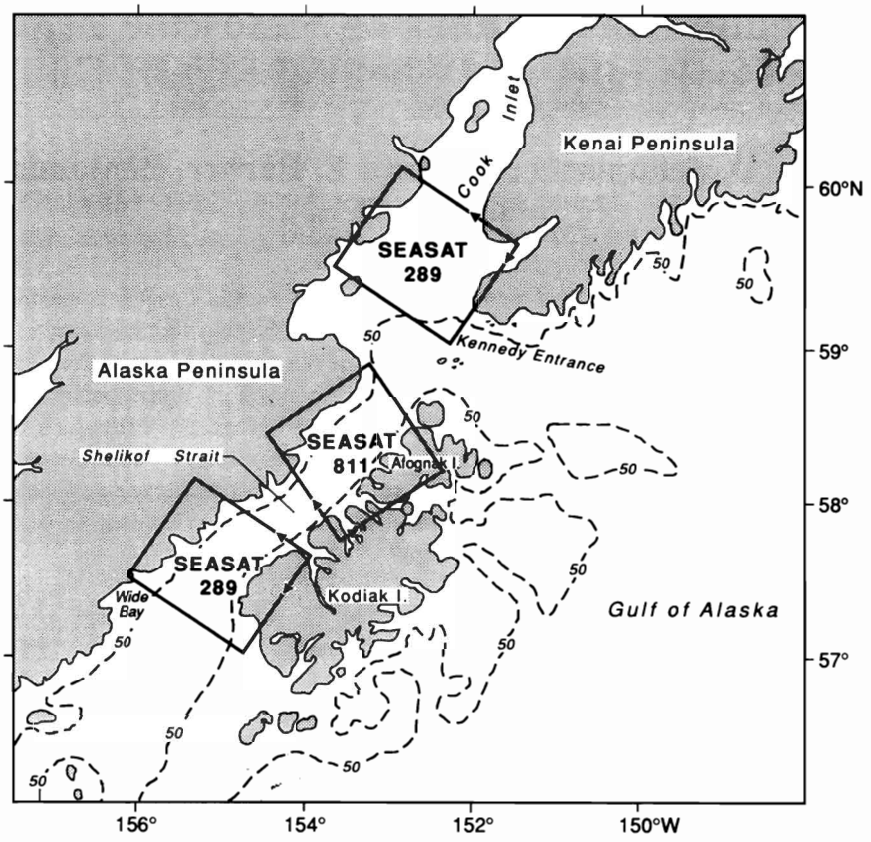

Fig. 1. The study region in the Gulf of Alaska. The locations of Seasat SAR imagery (shown in Figs. 3a, 4a, and 5) and the revolution numbers are indicated. Depth contours (dashed lines) are in fathoms (50 fathoms = 92 m).

The Seasat satellite, launched in summer 1978, carried an SAR. Although Seasat failed after 105 days in orbit, it provided extensive information that demonstrates the potential to examine and monitor upper oceanic processes. Phenomena revealed by Seasat SAR imagery include eddies, fronts, bathymetric features, surface and internal waves, windrows, and ships and their wakes (Fu and Holt, 1982). Data gathered by Seasat have also provided information to use in investigating the mechanisms responsible for these phenomena (Beal et al., 1981; Vesecky and Stewart, 1982; Fu and Holt, 1983). Thus, SAR may be a valuable tool to extend our capabilities in investigating oceanic processes and how they may affect recruitment to fisheries.

Much of the analysis of the utility of SAR for oceanographic studies has been done using imagery from Seasat (e.g., Fu and Holt, 1982; Beal et al., 1981; Vesecky and Stewart, 1982) and from the shuttle imaging radar (SIR) series in 1981 and 1984 (Cimino et al., 1988). SAR oceanographic studies have mostly emphasized the accuracy of surface wave directional and height spectrums (e.g., Hasselmann et al., 1985) and the observations of near-surface internal waves (e.g., Fu and Holt, 1984; Apel and Gonzalez, 1983; Liu, 1988; Gasparovich et al., 1988). Several studies have examined the SAR detection of currents and mesoscale circulation features such as the Gulf Stream and its warm-core eddies (Lichy et al., 1981; Hayes, 1981), cold eddies (Cheney, 1981), smaller-scale fronts and eddies (Fu and Holt, 1983), and wave-current interaction (e.g., Liu et al., 1989; Barnett et al., 1989; Johannessen et al., 1990). Mesoscale features are

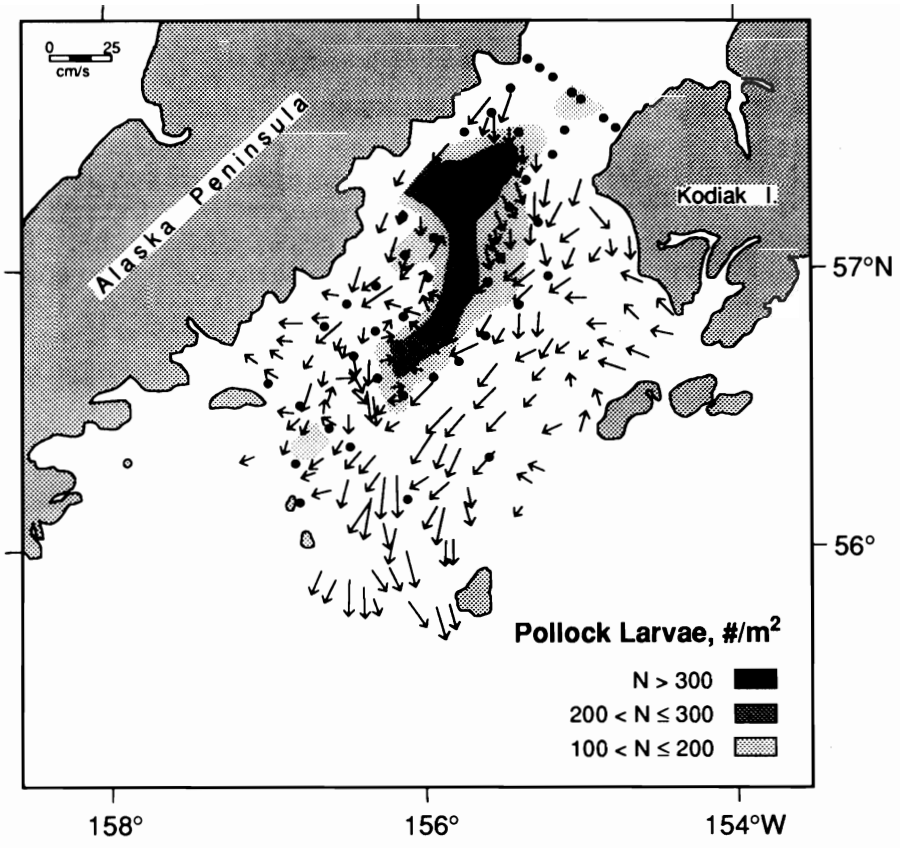

Fig. 2. Surface velocity field (cm s^{-1}) inferred from AVHRR images of sea surface temperature, and contours of larval abundance. The contours are in units of m^{-2} so that they are normalized by depth. The surface current distribution was made from tracking features from images on 28 and 29 April 1986.

imaged by SAR through several possible mechanisms that are not well understood. These mechanisms include the modulation of the short surface waves by current shear, the alteration of the stability of the surface wind across a relatively sharp sea surface temperature gradient, shifts in the Doppler frequency due to variability in the surface currents, and current-induced wave refraction. The SAR studies of oceanographic features have shown considerable promise for understanding the mesoscale dynamics of the ocean circulation, especially if used in combination with larger-scale satellite measurements such as from altimeters, scatterometers, and visible imaging satellite sensors (EOS SAR Panel, 1988).

In this report, we examine SAR imagery from several Seasat passes over the lower Cook Inlet/Shelikof Strait region of the Gulf of Alaska to assess the capability of SAR to detect mesoscale features of interest, including eddies, frontal current meanders, and internal waves in the northwest coastal region of Alaska. We compare the SAR imagery with imagery from AVHRR and from a Coastal Zone Color Scanner (CZCS), and with results of a radar scattering model, which incorporate in situ field measurements. Our objectives are (1) to determine the potential use of SAR in detecting features associated with physical processes in the study area, and (2) to integrate SAR information into the FOCI project. The satellite SAR may be a tool to aid in the management of fisheries and the development of recruitment models.

2. REGIONAL SETTING

All the satellite images we present are of lower Cook Inlet and Shelikof Strait. The dominant circulation feature there is the Alaska Coastal Current (ACC), which is driven by coastal convergence and freshwater flux along the Kenai Peninsula (Schumacher and Reed, 1980; Schumacher et al., 1989). The ACC enters lower Cook Inlet/Shelikof Strait through Kennedy Entrance, follows the 100-m isobath, and then flows southwestward through the Shelikof Strait along the sea valley. Baroclinic instability (Mysak et al., 1981) within the strait results in formation of meanders throughout and eddies at the southern exit. The eddies are translated toward the southwest and have been observed off Wide Bay (Incze et al., 1990). Within Cook Inlet, features of the mean circulation are (1) a band of southward flow along the western shore (with salt content diluted by river runoff), (2) a slow northward drift on the eastern side of the inlet, and (3) an intense westerly flow across the lower inlet along the 100-m and deeper isobaths (Muench et al., 1978). The third feature is the local manifestation of the ACC. The instantaneous current field is dominated by wind-driven currents and tidal currents that vary from prominent (principal lunar component, M2, amplitude of 80 cm s^{-1}) in the eastern lower inlet to weaker (M2 amplitude of 40 cm s^{-1}) in the central and western inlet (Muench and Schumacher, 1980; Isaji and Spaulding, 1987).

3. METHODS AND OBSERVATIONS

3.1. Satellite Observations

Seasat operated during the summer and early fall of 1978 (Fu and Holt, 1982). Because on-board tape recorder capacity was limited, SAR data could be acquired only when the satellite was in view of a ground receiving station. About 40 hours of SAR imagery was obtained over North America and Europe. Within Alaska, imagery was obtained at the Fairbanks station. Areal coverage was of the northeast Pacific south to about 50°N.

For this study, there were five separate Seasat passes that covered Cook Inlet and Shelikof Strait. We examined upper Shelikof Strait from SAR imagery revolution (Rev) 811 (22 August 1978), which shows a frontal current meander (Fig. 3a), and Cook Inlet imagery from Rev 289 (17 July 1978), which shows internal waves (Fig. 4a). Lower Shelikof Strait was also covered by imagery from Rev 289, which shows a pair of mesoscale eddies (Fig. 5). We also examined imagery from Rev 323 (20 July 1978), Rev 1284 (24 September 1978), and Rev 1499 (7 October 1978), which covered lower Cook Inlet, but these images contained no detectable ocean features of interest. One explanation for the lack of detectable features on these three passes is high winds. Several studies have shown that winds greater than about 10 m s^{-1} tend to obscure detectable ocean features on SAR (Fu and Holt, 1984; Lichy et al., 1981). Below a threshold (approximately 2 m s^{-1}), the short surface wave field is not adequately developed to produce images that contain mesoscale features of the ocean. Wind observations collected on five islands surrounding the coastal waters southwest of Kodiak Island indicate that wind speeds between 2 and 10 m s^{-1} occur from 40% to 80% of the time for any given month (Macklin, 1987; Macklin, PMEL, personal communication). During the months of May through July when larval and early juvenile pollack abound in the study area, the percentage of winds in the usable band increases to greater than 65% and up to 85%, depending on location. Another explanation for the lack of detectable features is that no mesoscale features were present. The SAR imagery has been digitally processed into 100 km × 100 km scenes and has been ground-corrected, which removes skewness due to imaging geometry.

Remotely sensed observations of the Shelikof Strait region were also gathered by National Oceanic and Atmospheric Administration (NOAA) satellites in 1988 using the AVHRR

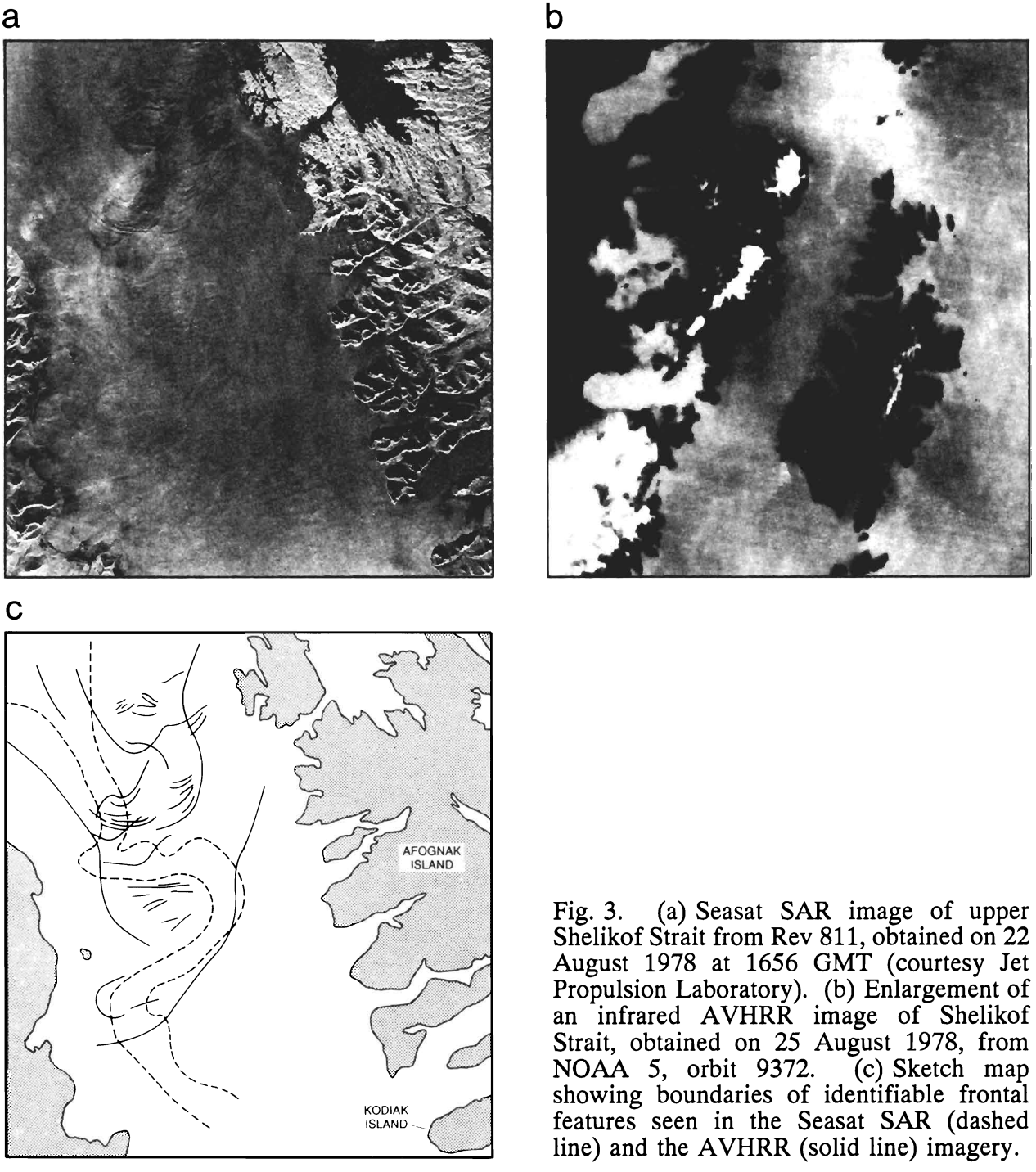

Fig. 3. (a) Seasat SAR image of upper Shelikof Strait from Rev 811, obtained on 22 August 1978 at 1656 GMT (courtesy Jet Propulsion Laboratory). (b) Enlargement of an infrared AVHRR image of Shelikof Strait, obtained on 25 August 1978, from NOAA 5, orbit 9372. (c) Sketch map showing boundaries of identifiable frontal features seen in the Seasat SAR (dashed line) and the AVHRR (solid line) imagery.

instruments and were obtained as High-Resolution Picture Transmission (HRPT) scenes from NOAA's National Environmental Satellite, Data, and Information Service (NESDIS). The present study uses full 1.1-km-resolution, channel 4 (11-μm-band) images processed from these scenes with a single-channel atmospheric correction and mapped to Mercator projections (Fig. 6a). Analysis of these images for advective sea surface flow estimates (Vastano and Reid, 1985) required measurement of sea surface temperature pattern displacements with sequential images using an interactive visualization algorithm (Vastano and Borders, 1984).

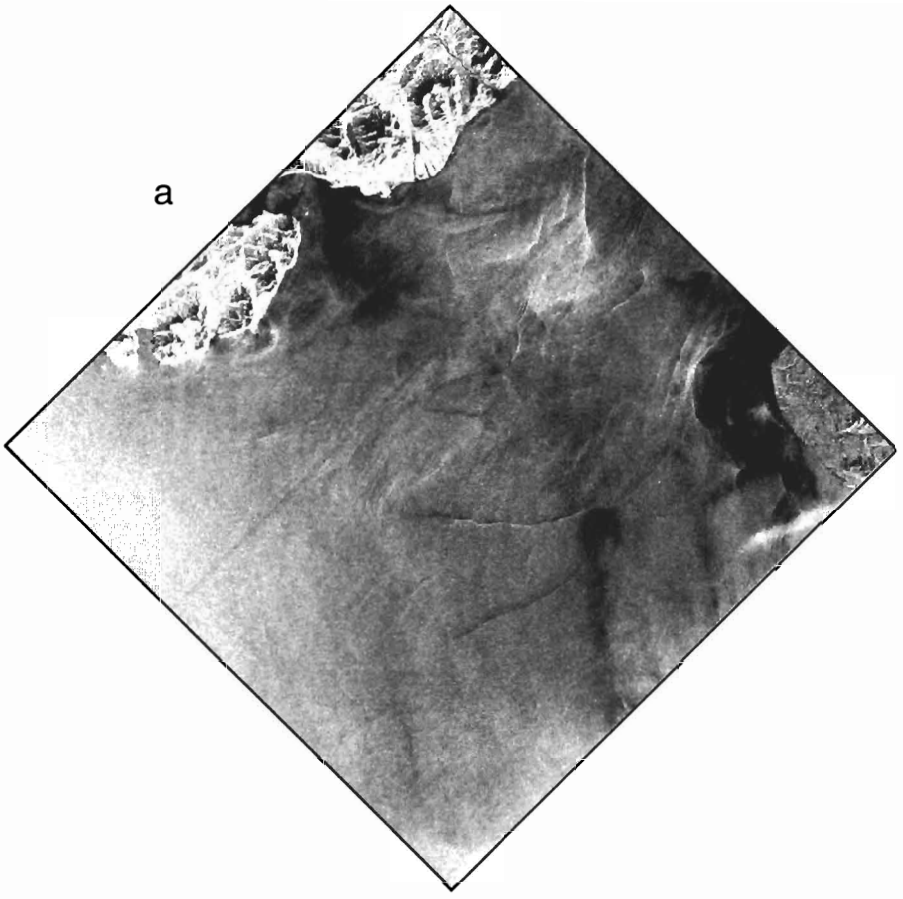

Fig. 4. (a) Seasat SAR image of lower Cook Inlet from Rev 289, obtained on 17 July 1978 at 0548 GMT (courtesy Jet Propulsion Laboratory).

Figure 7 shows derived pigment images obtained from the CZCS on the NIMBUS 7 satellite, which passed over the lower Shelikof Strait on 24 May 1986. The CZCS, like the AVHRR, cannot see the ocean surface through clouds. Bright clouds (and bright land) create anomalous signals (known as ringing) due to saturation of the sensor as it passes over them. Ringing occurs only on the right side of the cloud (or land), since the sensor scans left to right. The CZCS pigment image in Fig. 7a uses a color scale, in which land, clouds, and extremely high values are white. Pigment concentrations varying from low to high are represented by purple, dark blue, blue, green, yellow, orange, and red. The image was mapped to an earth grid. An eddy can barely be seen off Wide Bay, just to the south of the small white patch in the area of apparently very high pigment (this signal may be contaminated by land-ringing). Off the continental shelf, the pigment concentrations are low, as shown by the color blue. For some areas with high pigment, the clarity of mesoscale features may be enhanced by setting the water-leaving radiance band at 520 ± 10 nm, as shown in Fig. 7b for the same scene as in Fig. 7a. The anticyclonic eddy/swirl is more clearly seen in Fig. 7b. Although the color scale is different from that in Fig. 7a, it follows the same trend, with purples and blues representing low radiances and salmon colors representing higher radiances. North of the eddy/swirl, the ringing area is most noticeable next to land, but it is unclear how far to the east its effect persists. The location of the eddy/swirl in the CZCS image is consistent with locations of similar features in AVHRR, SAR, and in situ measurements from different times. General location and size are confirmed by biological and physical measurements (Incze et al., 1990) collected within about a week of the CZCS image.

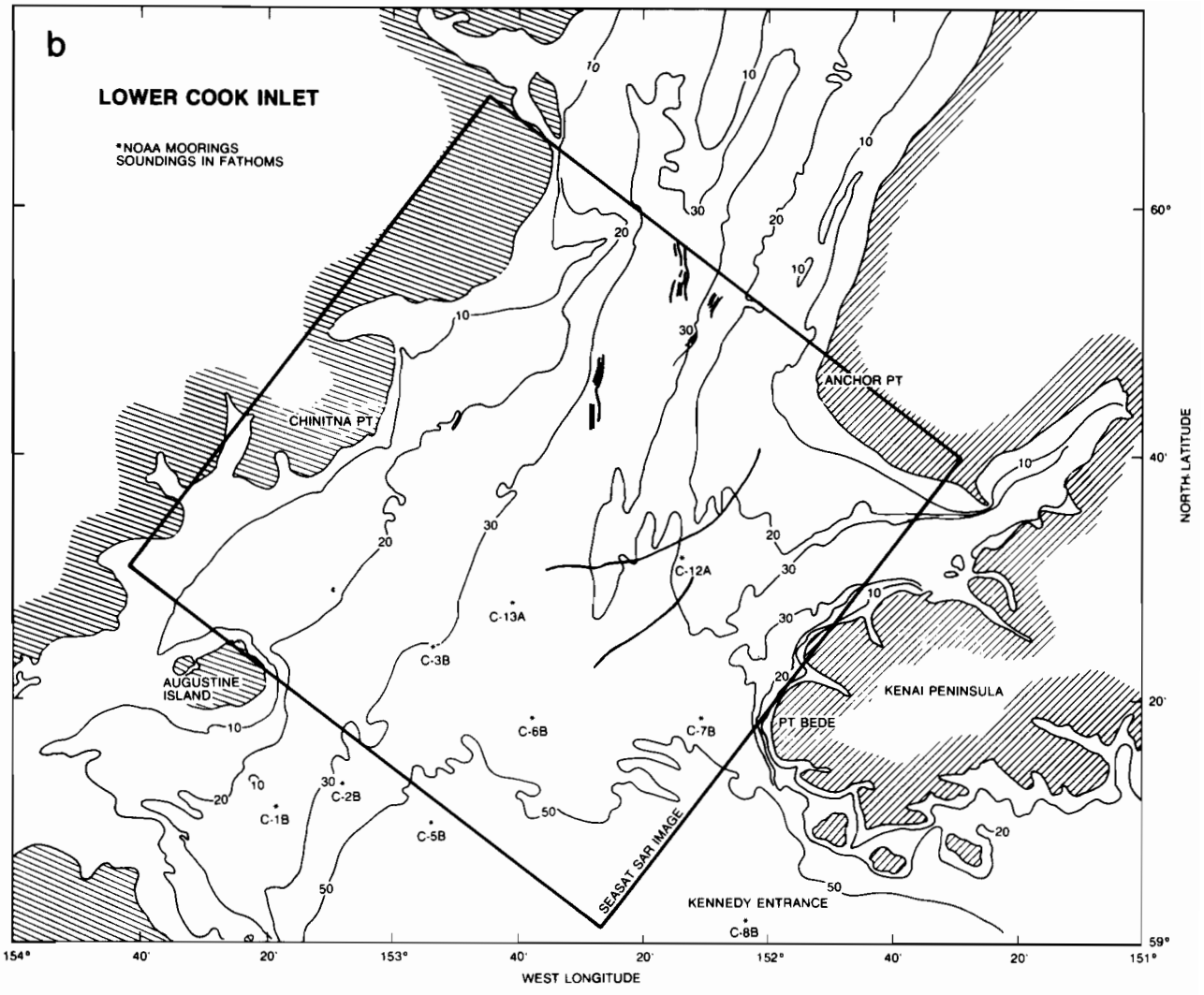

Fig. 4. (b) Bathymetry map (10 fathom contour interval) of lower Cook Inlet, indicating the locations of internal wave packets seen in the SAR image in Fig. 4a and the locations of moored current meters (asterisks) from summer 1978 (see also Fig. 8).

3.2. In Situ Measurements

Moored current meters were deployed using taut-wire moorings and acoustic releases. Aanderaa RCM-4 recording current meters were used on all moorings. These meters use Savonius rotors to measure current speed, and vane and compass assemblies for determining current direction. The current meters sampled at 15- or 20-min intervals. Raw data were low-pass filtered to remove high-frequency noise; this filter passed more than 99% of the amplitude at periods greater than 5 h, 50% at 2.86 h, and less than 0.5% at 2 h. This series was then further filtered to remove most of the tidal energy. The second filter passed more than 99% of the amplitude at periods of more than 55 h, 50% at 35 h, and less than 0.5% at 25 h. The second, low-pass-filtered series was then resampled at 6-h intervals and was used for examining nontidal circulation.

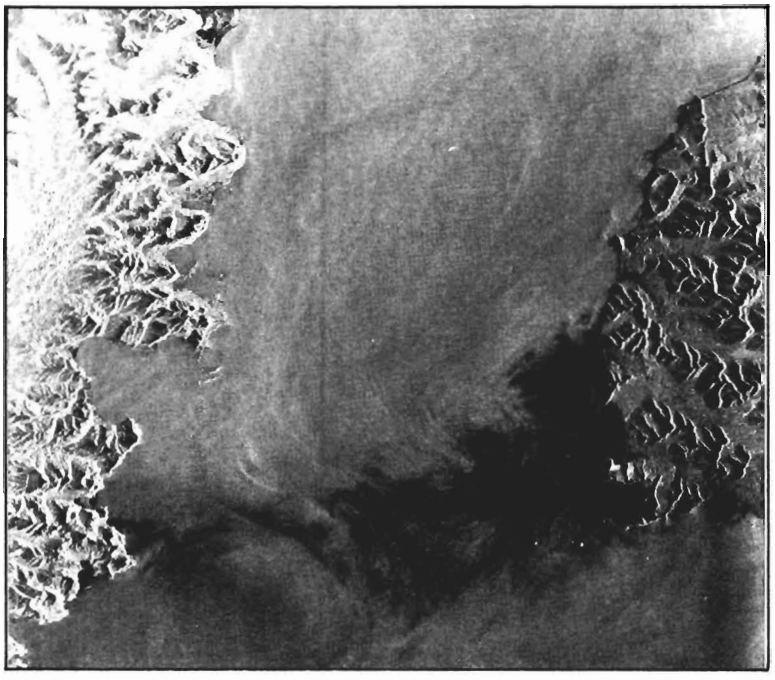

Fig. 5. Seasat SAR image of lower Shelikof Strait from Rev 289, obtained on 17 July 1978 at 0549 GMT (courtesy Jet Propulsion Laboratory). The sketch map of the mesoscale eddy in this image is shown in Fig. 6d.

Temperature and salinity data were obtained aboard ship using a Plessey Model 9040 conductivity/temperature/depth (CTD) profiling system during 1978 and a Sea Bird Electronics system during 1988. These data were recorded during the downcast, and descent rate was held to about 1 m s^{-1} or less to minimize error in the recorded data due to thermal lag in the sensors in regions where large vertical temperature gradients were present. Water samples were obtained and analyzed for conductivity and temperature at roughly half of the CTD stations to provide field correction offsets. The water samples were obtained using a rosette sampler equipped with calibrated reversing thermometers. Conductivity was measured aboard ship using a portable salinometer calibrated with standard seawater. These calibration data confirmed an overall accuracy for the CTD temperature and salinity values of ±0.02°C and ±0.02 practical salinity units (psu), respectively, for the Plessey data and ±0.01°C and ±0.01 psu for the Sea Bird Electronics data.

During summer 1978, 11 current moorings were deployed in lower Cook Inlet. A complete description of the experiment is given in Muench et al. (1981), and Reed and Schumacher (1987) interpret the data in light of more recent advances in understanding of regional oceanography. Mooring locations and mean currents are shown in Fig. 8, and current statistics are given in Table 1. The measurements confirm results from previous studies. The current vectors at moorings C-1B, C-2B, and C-3B, and to a lesser degree at mooring C-13A represent the concentrated outflow from lower Cook Inlet, while those at moorings C-7B, C-11B, and C-12A represent the weak mean inflow. The ACC is manifested as the strong flow at moorings C-5B, C-8B, and C-10B. Water properties vary across Cook Inlet; the most dilute water is on the western side (Fig. 9).

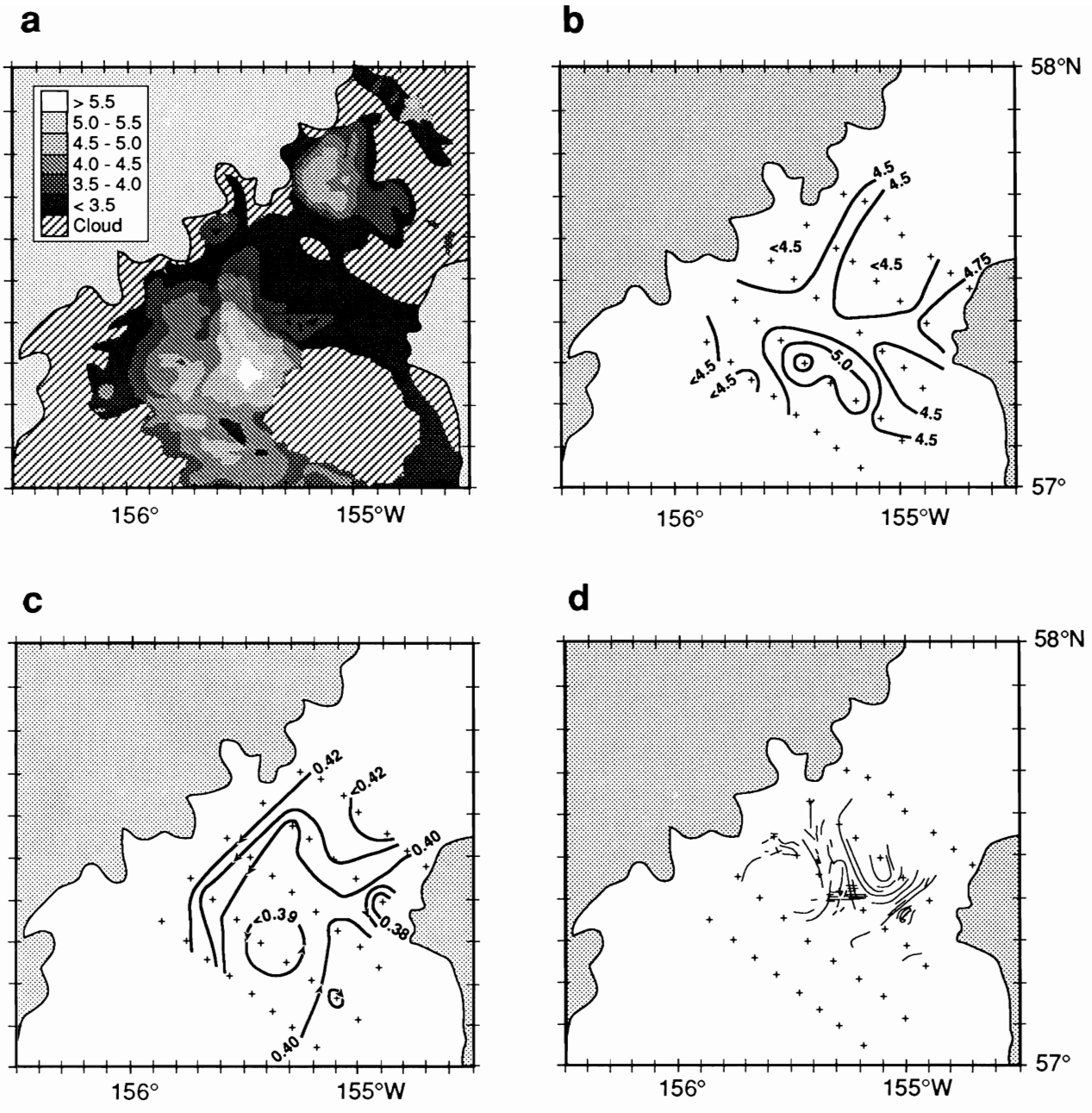

Fig. 6. (a) An interpretation of an AVHRR image of Shelikof Strait obtained on 29 April 1988, from NOAA 9 (orbit 17402, at 0047 GMT). The shaded temperature scale ranges from <3.5° to >5.5°C and shows cloud cover. (b) Sea surface temperature (°C) and (c) geopotential topography (dyn m), both derived from a 38-station (crosses) CTD survey that took place on 27–29 April 1988. (d) Sketch map of detectable current features seen in the eddy in the SAR image in Fig. 5.

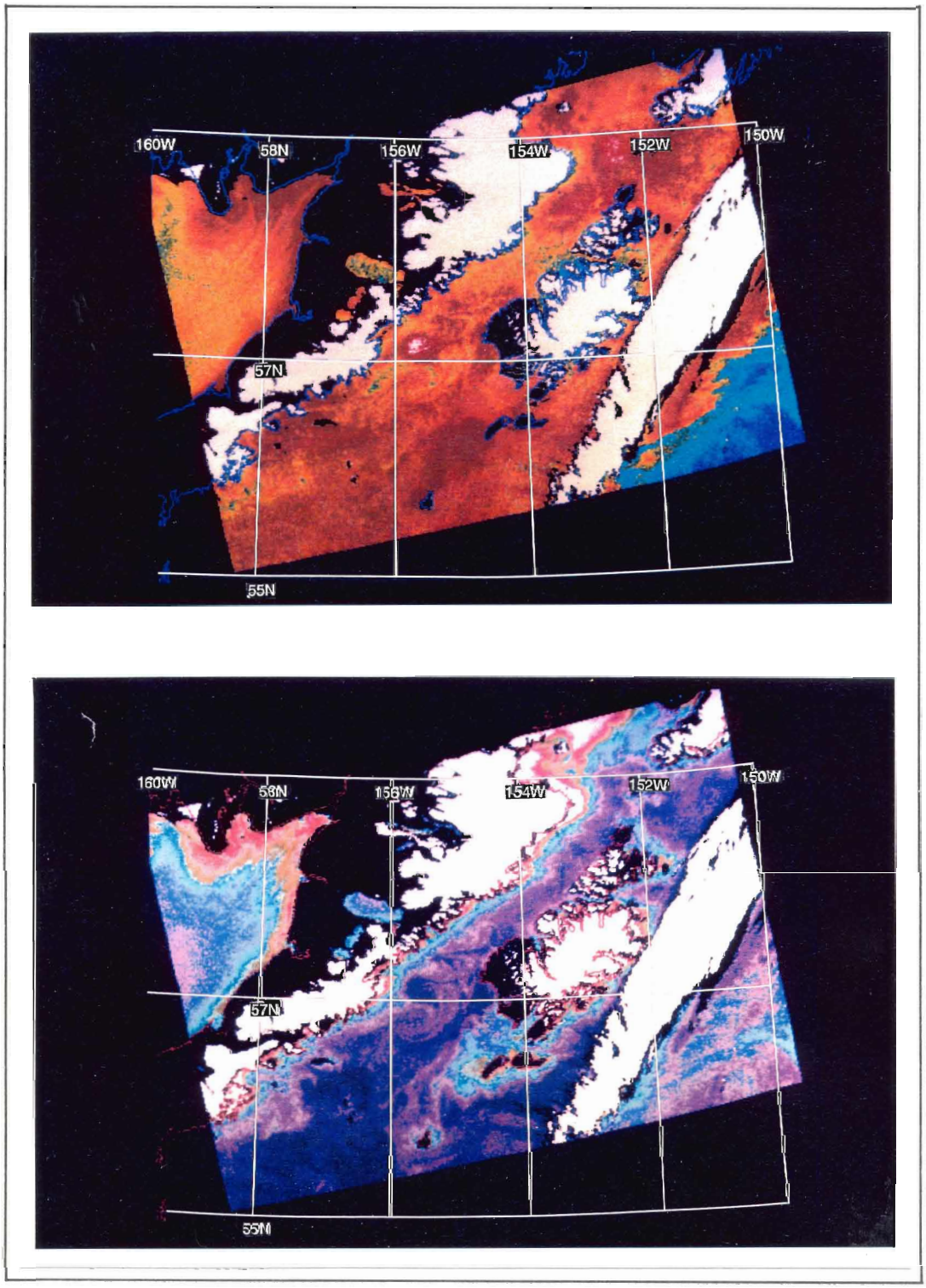

Fig. 7. A CZCS four-band composite pigment image (top) and the same image constructed using the radiance band at 520 nm (bottom). The data were collected by Nimbus 7 on 24 May 1986. Land, clouds, and extremely high radiance values are white; low radiances are represented by purples and blues, and higher radiances by salmon.

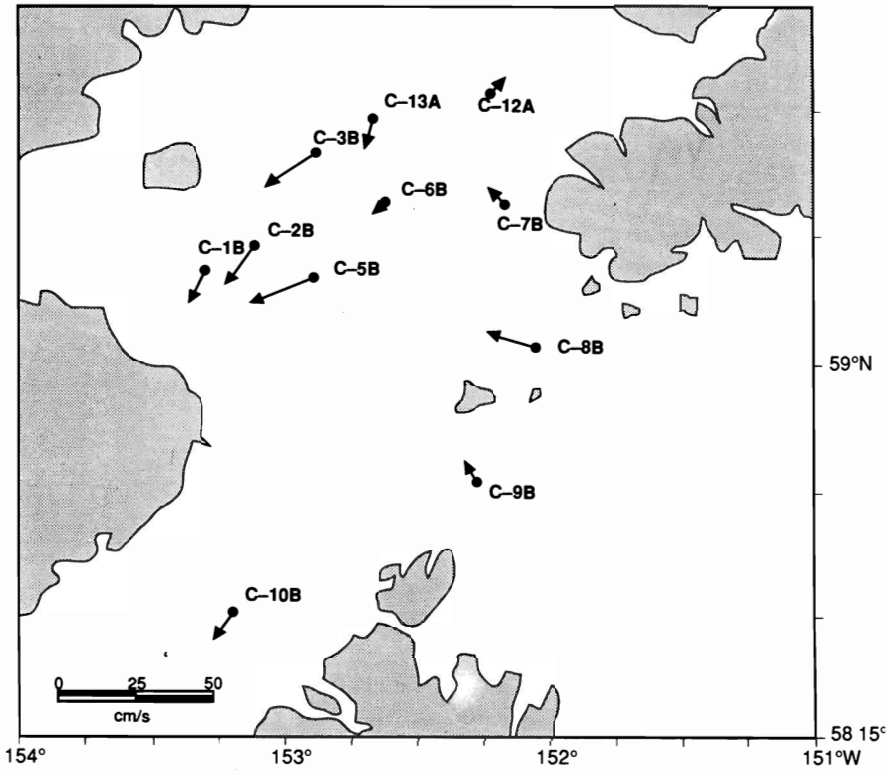

Fig. 8. Vectors showing mean currents (cm s^{-1}) at the 11 current moorings in the study area for the period 6 June–11 August 1978.

Table 1. Mooring information and mean current data for summer 1978

Mooring name	Observation period (JD)	Instrument depth (m)	Mean current speed ± RMS error* (cm s^{-1})	Mean current direction (°T)
C-1B	149–235	18	9.9 ± 1.5	202
C-2B	148–291	18	14.4 ± 1.8	217
C-3B	148–291	25	17.8 ± 1.5	236
C-5B	148–264	27	18.7 ± 5.2	251
C-6B	148–292	26	1.4 ± 0.9	215
C-7B	148–291	17	3.8 ± 0.8	309
C-8B	141–277	63	13.1 ± 2.3	283
C-9B	149–288	63	5.0 ± 1.7	296
C-10B	149–283	25	10.5 ± 2.0	217
C-12A	148–229	20	3.9 ± 0.6	039
C-13A	149–290	27	7.7 ± 1.1	199

The longest simultaneous observation period for all moorings was JD157–JD223.

* RMS error is the square root of the record variance divided by the ratio of record length to integral time scale.

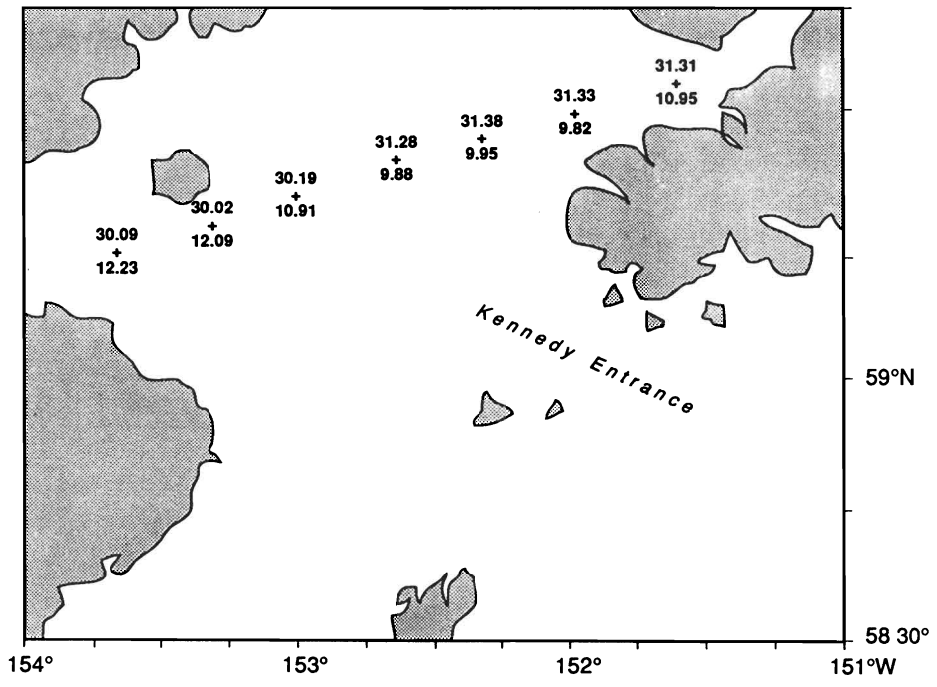

Fig. 9. Salinity (upper number, psu) and temperature (lower number, °C) at the surface of lower Cook Inlet on 17 August 1978.

4. RESULTS

4.1. Internal Wave Features

The Seasat SAR imagery of internal waves, collected over lower Cook Inlet during Rev 289 on 17 July 1978, is shown in Fig. 4 with interpretive line drawings of the internal waves. A series of internal wave packets is visible in the middle of the SAR image. Each wave is characterized by a bright band followed immediately by a dark band. These features are probably generated by the tide interacting with features of the bottom. Although no "sea-truth" is available for the present case, the identification as internal waves is quite certain (e.g., Liu, 1983) and has been verified in field tests in the New York Bight (Liu, 1988). There are several characteristics of the sea surface pattern induced by the internal waves. The important ones are summarized as follows:

(1) The internal waves occurred in packets, separated by distances that are approximately 20 km.
(2) On the basis of the assumption that the wave packets were generated by the semidiurnal tidal current, their estimated speed was 0.50 m s^{-1}.
(3) The wave packets in this region contained about seven waves with a packet width of about 4 km.
(4) Within a given wave packet, the wavelengths appeared to decrease monotonically, front to rear, and the surface pattern is always more observable at the front of the wave packet than at the rear.
(5) The wave packet propagation direction was refracted by the current and evolved as it propagated through lower Cook Inlet.

These features suggest that the internal waves in each packet were probably rank-ordered solitary waves with the largest, fastest, and longest waves in front. We can examine our assumption that the internal waves were generated by the semidiurnal tidal current. Water property data were collected at several stations in central lower Cook Inlet within a day of Rev 289. The average mixed-layer depth was 30 m in a water column 100 m deep, and the difference in density between the two layers was approximately 1.0×10^{-3}. Using these observations in an equation for internal waves,

$$v_g = \left(g' \frac{h_1 h_2}{H} \right)^{1/2} ,$$

where g′ is the reduced gravity $g(\Delta\rho/\rho)$, $\Delta\rho$ is the density difference between lower and upper layers and ρ is the mean density of the two layers, h_1 and h_2 are the depths of the upper and lower layers, and H is the overall water column depth, gives a group velocity v_g of 0.45 cm s^{-1}. The close agreement between wave speeds from the model and those estimated from the SAR image supports our contention that the wave packets were generated by the vigorous semidiurnal tidal currents extant in lower Cook Inlet.

The essential element of the surface effects of the SAR backscattering is the interaction between the internal-wave-induced surface current field and the wind-driven ocean surface waves (Liu, 1983; Caponi et al., 1988). Basically, the wave-current interaction is based on a near-equilibrium spectral transport model to estimate the roughness modulation by a variable surface current. The effect of surface current is to alter the spectrum from its equilibrium value while the natural processes of wave energy input from the wind, wave breaking, and other non-conservative processes act to restore the ambient equilibrium spectrum. To observe internal waves in the coastal region, the strain rate (horizontal shear stress) must be of order 10^{-3} s^{-1} (Liu, 1988).

4.2. Meanders

One Seasat SAR image (Rev 811, Fig. 3a) shows a cold-water filament meandering in the upper Shelikof Strait on 22 August 1978. For comparison, an AVHRR image from Rev 9372 (25 August 1978) at the same location is shown in Fig. 3b. In the AVHRR image, the cold-water mass flowing into upper Shelikof Strait had surface temperature differences between the meander and adjacent water of 1°–2°C. Such differences are consistent with observations of horizontal surface temperature gradients in lower Cook Inlet (e.g., Fig. 9). The surface signature in the SAR image is very likely caused by the effects of an air-sea temperature difference on sea surface roughness. Basically, the cold water stabilizes the atmosphere boundary layer. Variations in the stable atmospheric density stratification, as a result of air-sea temperature differences, can dampen the turbulent momentum exchange rate in the boundary layer and later the velocity profile near the ocean surface. This altered wind velocity profile may significantly change the energy transfer rate from the wind to the ocean surface waves. The dampened surface waves and roughness modulation at cold-water regions show as a dark band in the SAR imagery.

The air-sea interaction model for atmospheric stability effects on surface wave modulation was reported by Chen et al. (1986); the model was based on the model by Large and Pond (1981). Chen et al. show friction velocity as a nonlinear function of wind speed and air-sea temperature difference. The friction velocity u_*, defined as the square root of turbulent shear stress divided by air density, is a measure of the turbulent momentum flux. Since the friction velocity is directly related to the wind stress, it is closely related to the radar cross section, as

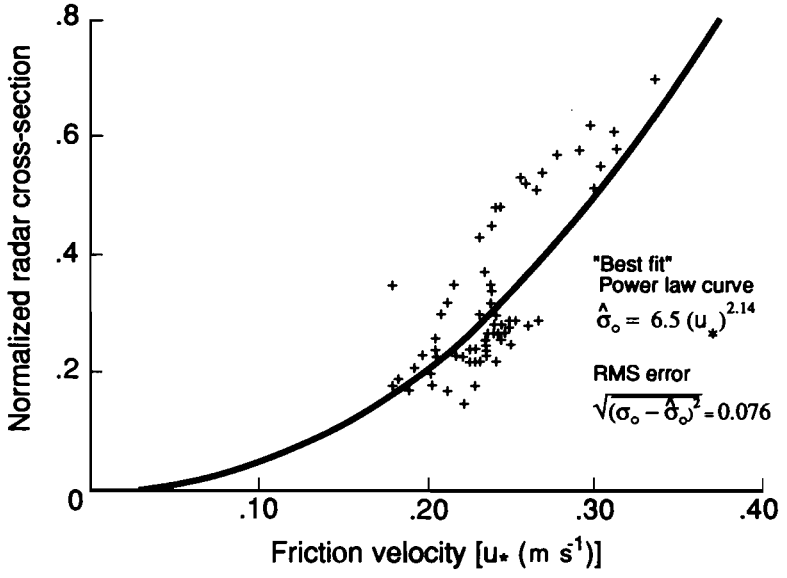

Fig. 10. Radar cross section data values (for stable atmospheric conditions) and model function from a power law fit, versus friction velocity (slope values ignored). Error is the root mean square of residual. [Data are a subset from Keller et al. (1985, Fig. 7b).]

shown in Fig. 10, under stable conditions (Weissman, 1987). The best fit to data from Keller et al. (1985) represents a power law curve as a transfer function model. As an example, in the upper Shelikof Strait the air-sea temperature difference is approximately 1°–2°C. From Fig. 10, with an assumed wind speed of 6 m s^{-1}, the friction velocity is 19 cm s^{-1} for the neutral condition (corresponding to the surrounding environment with no air-sea temperature difference) and is 17 cm s^{-1} for the stable condition. Also from Fig. 10, the normalized radar cross section is 0.2 for the neutral condition and 0.15 for the stable condition. A change (reduction) of radar cross section by 25% due to the cold-water flow into the upper Shelikof Strait is a reasonable estimate. For weaker wind speed (4 m s^{-1}), the change of radar cross section is larger (by a factor of 2), and the SAR intensity contrast is also larger.

4.3. Eddies

Figure 5 shows a Seasat SAR image of eddies collected over the lower Shelikof Strait during Rev 289 (17 July 1978). The dark region behind Kodiak Island is caused by low radar backscattering from a smooth ocean surface. The relatively smooth surface may be due either to the surface slick or to wind shadowing by the island. Small vortices are barely observable behind the island. A pair of eddies, however, can be identified in the lower Shelikof Strait near the Alaska Peninsula. Dipole or pairs of eddies have also been identified in Landsat Thematic Mapper data of the Alaska Coastal Current about 700 km upstream from the pair in Shelikof Strait (Ahlnäs et al., 1987). In the present study area, eddies have been shown in AVHRR, CZCS, and in situ measurements from different times (e.g., Fig. 6).

The generation mechanisms for eddies in this region are not well understood. Eddies may be caused by the baroclinic instability in Shelikof Strait or by complex patterns in surface winds (Schumacher et al., 1989). It is important to note that the eddy in the 1986 AVHRR (cold ring) and CZCS images is anticyclonic, whereas the eddy in the 1988 AVHRR (warm ring) and in situ

measurements (Fig. 6) is cyclonic. During May 1990, three satellite-tracked buoys, drogued at 40 m, were deployed in a region with a high abundance of pollack larvae. All three buoys circulated in an anti-cyclonic eddy for approximately 10 days before dispersing. The cause of different rotational directions and their implication for formation mechanisms and larval retention are not currently known.

5. DISCUSSION

We have compelling evidence that a wide range of scales of eddies are detectable in SAR imagery in Shelikof Strait. SAR imagery from Seasat demonstrated that mesoscale eddies can be detected by their influences on the short gravity waves responsible for microwave radar backscatter. The mechanisms that alter the short gravity wave field in that area are not well understood. In at least some situations, it is likely that current gradients near the boundary of an eddy modify the spectrum of short waves, similar to the internal wave packets, producing the microwave backscatter. In other instances, or perhaps concurrently, sea-state change can also be induced by sea surface temperature variations that alter the atmospheric boundary layer stability. This gives rise to local variation in wind stress that is similar to the process apparently induced by the meander observed in upper Shelikof Strait.

It is important to understand the generation processes and persistence of these eddies and variability of their characteristics. Through efforts to gain better understanding of these features we may also gain better understanding of how the regional environment affects survival of larval pollock and their eventual recruitment into the commercial fishery. Future research in FOCI will emphasize field studies that match space and time scales of circulation with biological processes. SAR would be a good tool to monitor the evolution of mesoscale eddies. During the next 5 years, three spacecraft will carry SAR in near-polar orbits. These satellites are the first European Remote Sensing Satellite (ERS 1), the Japanese first Earth Resources Satellite (J-ERS 1), and RADARSAT to be flown by the Canada Centre for Remote Sensing (CCRS). In collaboration with these satellite programs, NASA has instructed the Jet Propulsion Laboratory (JPL) and the University of Alaska at Fairbanks to design, implement, and operate an Alaska SAR Facility (ASF) ground station at Fairbanks to receive and process the SAR data from ERS 1. A program is also to be developed that utilizes the data effectively in a wide variety of scientific disciplines. Because of the special capabilities of SAR systems, it is anticipated that applications of SAR for fisheries oceanography will emerge following the launch of ERS 1 in April 1991.

6. ACKNOWLEDGMENTS

The authors thank Tom George (University of Alaska) for supplying the 1978 AVHRR image, Kristina Ahlnäs (University of Alaska) for providing sea surface temperature estimates for the same period, and John Crawford (JPL) for image co-registration. A.K. Liu extends thanks to Jane Elrod (NASA) for providing the CZCS images. We thank D. Vastano (Texas A&M University) and T. Vance (PMEL) for the surface current vectors and AVHRR images from 1988. Some of the graphic work was provided by Karen Conlan (PMEL), and we thank Christy Sweet (ERL) for thorough technical editing. Portions of this work were performed at the Jet Propulsion Laboratory, California Institute of Technology, under contract to the National Aeronautics and Space Administration. The work performed by A.K. Liu was supported by the NASA Oceanic Processes Program and that of W.E. Barber by the University of Alaska, Fairbanks. This work was partially funded by NOAA's Fisheries Oceanography Coordinated Investigations and is FOCI contribution No. 0112 and PMEL contribution No. 1230.

7. REFERENCES

Ahlnäs, K., T.C. Royer, and T.H. George, 1987. Multiple dipole eddies in the Alaska Coastal Current detected with Landsat Thematic Mapper data. *J. Geophys. Res. 92*(C12): 13,041–13,047.

Apel, J.R., and F.I. Gonzalez, 1983. Nonlinear features of internal waves off Baja California as observed from the Seasat imaging radar. *J. Geophys. Res. 88*:4459–4466.

Barnett, T.P., F. Kelly, and B. Holt, 1989. Estimation of the two-dimensional ocean current shear field with a synthetic aperture radar. *J. Geophys. Res. 94*(C11):16,087–16,095.

Beal, R.C., P.S. DeLeonibus, and I. Katz (Eds.), 1981. *Spaceborne Synthetic Aperture Radar for Oceanography*. Johns Hopkins University Press, Baltimore, MD, 215 pp.

Caponi, W.A., D.R. Crawford, H.C. Yuan, and P.G. Saffman, 1988. Modulation of radar backscatter from the ocean by a variable surface current. *J. Geophys. Res. 93*: 12,249–12,263.

Chen, S.H., A.K. Liu, and T. Kubota, 1986. Atmospheric stability effects of surface wave modulations. DTN-8607-03, Dynamics Technology, Torrance, CA, 47 pp.

Cheney, R.E., 1981. A search for cold water rings. In *Spaceborne Synthetic Aperture Radar for Oceanography*, R.C. Beal, P.S. DeLeonibus, and I. Katz (Eds.). Johns Hopkins University Press, Baltimore, MD, 161–170.

Cimino, J.B., B. Holt and A. Richardson, 1988. The Shuttle Imaging Radar-B (SIR-B) Experiment report. JPL Publication 88–2, Documentation Group, Jet Propulsion Laboratory, Pasadena, CA, 218 pp.

EOS SAR Panel, 1988. Earth Observing System Instrument Panel report IIF—Synthetic aperture radar. National Aeronautics and Space Administration, Washington, DC, 233 pp.

Fu, L.L., and B. Holt, 1982. Sea ice with synthetic aperture radar. JPL Publication 81-120, Jet Propulsion Laboratory, Pasadena, CA, 200 pp.

Fu, L.L., and B. Holt, 1983. Some examples of detection of oceanic mesoscale eddies by the Seasat synthetic aperture radar. *J. Geophys. Res. 88*:1844–1852.

Fu, L.L., and B. Holt, 1984. Internal waves in the Gulf of California: Observations from a spaceborne radar. *J. Geophys. Res. 89*:2053–2060.

Gasparovich, R.F., J.R. Apel, and E.S. Kasischke, 1988. An overview of the SAR Internal Wave Signature Experiment. *J. Geophys. Res. 93*:12,304–12,316.

Hasselmann, K., R.K. Raney, W.J. Plant, W. Alpers, R.A. Shuchman, D.R. Lyzenga, C.L. Rufenach, and M.J. Tucker, 1985. Theory of synthetic aperture radar ocean imaging: A MARSEN view. *J. Geophys. Res. 90*:4659–4686.

Hayes, R.M., 1981. Detection of the Gulf Stream. In *Spaceborne Synthetic Aperture Radar for Oceanography*, R.C. Beal, P.S. DeLeonibus, and I. Katz (Eds.). Johns Hopkins University Press, Baltimore, MD, 146–160.

Hinckley, S., K. Bailey, S. Piquelle, J. Schumacher, and P. Stabeno, 1991. Transport, distribution, and abundance of larval and juvenile walleye pollock (*Theragra chalcogramma*) in the western Gulf of Alaska in 1987. *Can. J. Fish. Aquat. Sci. 48*:91–98.

Incze, L.S., P. Ortner, and J.D. Schumacher, 1990. Microzooplankton, vertical mixing and advection in a larval fish patch. *J. Plankt. Res. 12*:365–379.

Isaji, I., and M.L. Spaulding, 1987. A numerical model of the M_2 and K_1 tide in the northwestern Gulf of Alaska. *J. Phys. Oceanogr. 17*:698–704.

Johannessen, J.A., R.A. Schuchman, O.M. Johannessen, and K. Davidson, 1990. NORCSEX '88: A pre-launch satellite study of SAR imaging capabilities of upper ocean circulation features and wind fronts. Proceedings, IGARSS '90, University of Maryland, 20–24 May 1990. Institute of Electrical and Electronics Engineers, College Park, MD, 707–710.

Keller, W.C., W.J. Plant, and D.E. Weissman, 1985. The dependence of X-band microwave sea return on atmospheric stability and sea state. *J. Geophys. Res. 90*:1019–1029.

Large, W.G., and S. Pond, 1981. Open ocean momentum flux measurements in moderate to strong winds. *J. Phys. Oceanogr. 11*:324–336.

Lichy, D.E., M.G. Mattie, and L.J. Mancini, 1981. Tracking of a warm water ring. In *Spaceborne Synthetic Aperture Radar for Oceanography*, R.C. Beal, P.S. DeLeonibus, and I. Katz (Eds.). Johns Hopkins University Press, Baltimore, MD, 171–182.

Liu, A.K., 1983. Detection study of bottom features on Seasat synthetic aperture radar imagery. DT-8312-01, Dynamics Technology, Torrance, CA, 45 pp.

Liu, A.K., 1988. Analysis of nonlinear internal waves in the New York Bight. *J. Geophys. Res. 93*:12,317–12,329.

Liu, A.K., F.C. Jackson, E.J. Walsh, and C.Y. Peng, 1989. A case study of wave-current interaction near an oceanic front. *J. Geophys. Res. 94(C11)*:16,189–16,200.

Macklin, S.A., 1987. Coastal winds of the southeast Alaska Peninsula. NOAA Tech. Memo. ERL PMEL-73 (NTIS PB87-206173), NOAA Pacific Marine Environmental Laboratory, Seattle, WA, 131 pp.

Muench, R.D., and J.D. Schumacher, 1980. Physical oceanographic and meteorological conditions in the northwest Gulf of Alaska. NOAA Tech. Memo. ERL PMEL-22 (NTIS PB81-199473), NOAA Pacific Marine Environmental Laboratory, Seattle, WA, 147 pp.

Muench, R.D., H.O. Mofjeld, and R.L. Charnell, 1978. Oceanographic conditions in lower Cook Inlet: Spring and summer 1978. *J. Geophys Res. 83*:5090–5098.

Muench, R.D., J.D. Schumacher, and C.A. Pearson, 1981. Circulation in lower Cook Inlet, Alaska. NOAA Tech. Memo. ERL PMEL-28 (NTIS PB82-126418), NOAA Pacific Marine Environmental Laboratory, Seattle, WA, 26 pp.

Mysak, L.A., R.D. Muench, and J.D. Schumacher, 1981. Baroclinic instability in a downstream varying channel: Shelikof Strait, Alaska. *J. Phys. Oceanogr. 11*:950–969.

Reed, R.K., and J.D. Schumacher, 1987. Physical oceanography. In *The Gulf of Alaska, Physical Environment and Biological Resources*, D.W. Hood and S.T. Zimmerman (Eds.). (NTIS PB87-103230), U.S. Government Printing Office, Washington, DC, 57–75.

Reed, R.K., J.D. Schumacher, and A.W. Kendall, Jr., 1988. NOAA's Fisheries Oceanography Coordinated Investigations in the western Gulf of Alaska. *Eos, Trans. Am. Geophys. Union 69*:890–894.

Reed, R.K., L.S. Incze, and J.D. Schumacher, 1989. Estimation of the effects of flow on dispersion of larval pollock, *Theragra chalcogramma*, in Shelikof Strait, Alaska. *Can. Sp. Publ. Fish. Aquat. Sci. 108*:239–245.

Rothchild, B.J., 1986. *Dynamics of Marine Fish Populations.* Harvard University Press, Cambridge, MA, 277 pp.

Royer, T.C., and R.D. Muench, 1977. On the temperature distribution in the Gulf of Alaska, 1874–75. *J. Phys. Oceanogr. 7*:92–99.

Schumacher, J.D., and R.K. Reed, 1980. Coastal flow in the northwest Gulf of Alaska: The Kenai Current. *J. Geophys. Res. 85*:6680–6688.

Schumacher, J.D., P.J. Stabeno, and A.T. Roach, 1989. Volume transport in the Alaska Coastal Current. *Contin. Shelf Res. 12*:1071–1083.

Vastano, A.C., and S.E. Borders, 1984. Sea surface motion over an anticyclonic eddy on the Oyashio front. *Remote Sens. Environ. 16*:87–90.

Vastano, A.C., and R.O. Reid, 1985. Sea surface topography estimation with infrared satellite imagery. *J. Atmos. Technol. 2*:393–400.

Vastano, A.C., L.S. Incze, and J.D. Schumacher, 1991. Environmental and larval pollock observations at Shelikof Strait, Alaska. Unpublished manuscript.

Vesecky, J.F., and R.H. Stewart, 1982. The observation of ocean surface phenomena using imagery from the Seasat synthetic aperture radar: An assessment. *J. Geophys. Res. 87*(C5):3397–3430.

Weissman, D.E., 1987. Modeling the interactions between the ocean and the environment for microwave radar sensing. *Radio Sci. 22*:87–99.